Hou, Nianjun; Gan, Juanjuan; Yan, Qisheng; Zhao, Yicheng; Li, Yongdan

Improved electrochemical oxidation kinetics of $La_{0.5}Ba_{0.5}FeO_{3-\delta}$ anode for solid oxide fuel cells with fluorine doping

Published in:
Journal of Power Sources

DOI:
10.1016/j.jpowsour.2021.230932

Published: 15/02/2022

Document Version
Peer-reviewed accepted author manuscript, also known as Final accepted manuscript or Post-print

Please cite the original version:
Hou, N., Gan, J., Yan, Q., Zhao, Y., & Li, Y. (2022). Improved electrochemical oxidation kinetics of $La_{0.5}Ba_{0.5}FeO_{3-\delta}$ anode for solid oxide fuel cells with fluorine doping. *Journal of Power Sources*, *521*, Article 230932. https://doi.org/10.1016/j.jpowsour.2021.230932

Improved electrochemical oxidation kinetics of $La_{0.5}Ba_{0.5}FeO_{3-\delta}$ anode for solid oxide fuel cells with fluorine doping

Nianjun Hou[a,b], Juanjuan Gan[a,b], Qisheng Yan[a,b], Yicheng Zhao[a,b*], Yongdan Li[a,b,c]

[a]*State Key Laboratory of Chemical Engineering (Tianjin University), Tianjin Key Laboratory of Applied Catalysis Science and Technology, School of Chemical Engineering and Technology, Tianjin University, Tianjin, 300072, China*

[b]*Collaborative Innovation Center of Chemical Science and Engineering (Tianjin), Tianjin, 300072, China*

Email: zhaoyicheng@tju.edu.cn

[c]*Department of Chemical and Metallurgical Engineering, Aalto University, Kemistintie 1, FI-00076 Aalto, Finland*

*Email: zhaoyicheng@tju.edu.cn

Abstract

Sluggish anode kinetics and serious carbon deposition are two major obstacles to developing hydrocarbon fueled solid oxide fuel cells. A highly active and stable perovskite $La_{0.5}Ba_{0.5}FeO_{3-\delta}$ anode material is studied in this work. The oxygen surface exchange and charge transfer steps are the rate-determining steps of the anode process, and the former is accelerated with fluorine doping on the anion sites due to the lowering of metal-oxygen bond energy. The oxygen surface exchange coefficients of $La_{0.5}Ba_{0.5}FeO_{3-\delta}$ and $La_{0.5}Ba_{0.5}FeO_{2.9-\delta}F_{0.1}$ at 850 °C are 1.4×10^{-4} and 2.8×10^{-4} cm s^{-1}, respectively. A single cell supported by a 300 μm-thick $La_{0.8}Sr_{0.2}Ga_{0.8}Mg_{0.2}O_{3-\delta}$ electrolyte layer with $La_{0.5}Ba_{0.5}FeO_{3-\delta}$ anode shows maximum power densities of 1446 and 691 mW cm^{-2} at 850 °C with wet hydrogen and methane fuels, respectively, which increase to 1860 and 809 mW cm^{-2} respectively when $La_{0.5}Ba_{0.5}FeO_{2.9-\delta}F_{0.1}$ is used as the anode. The cell exhibits a short-term durability of 40 h using wet methane as fuel without carbon deposition on the anode.

Keywords: Anode; Solid oxide fuel cell; Anion doping; Hydrocarbon fuel; Lanthanum ferrite

1. Introduction

The development of innovative energy conversion and storage systems is highly demanded to meet the challenge of global warming and the gradual exhaustion of non-renewable fossil fuels. Solid oxide fuel cells (SOFCs) convert chemical energy of fuels into electricity directly with high efficiency and flexibility, which have attracted much attention as a promising power generation device [1, 2]. The high operating temperature (600-1000 °C) of SOFCs allows the utilization of low-cost and more available hydrocarbon fuels. Compared with other hydrocarbon fuels, methane has a high H/C ratio of 4. Accordingly, less CO_2 is emitted when methane is used as the fuel. Therefore, the direct utilization of methane with abundant reserves as the fuel of SOFC is favourable [3].

Conventional Ni-based cermet anode materials exhibit excellent catalytic activity and high electrical conductivity. However, the application of those anodes is hindered by serious agglomeration of metal nanoparticles at high operating temperatures (800-1000 °C) and coking when fueled with hydrocarbons [4]. Oxygen-deficient perovskites with a general formula $ABO_{3-\delta}$ are considered as one of the most promising anode materials for SOFCs with high coking resistance and sulfur tolerance to replace Ni-based anodes [5]. In 2003, Tao and Irvine [6] reported $La_{0.75}Sr_{0.25}Cr_{0.5}Mn_{0.5}O_{3-\delta}$ as a redox-stable anode, which exhibits polarization resistances (R_p) of 0.26 and 0.87 Ω cm^2 at 900 °C with wet H_2 (~3% H_2O) and wet CH_4 as fuels, respectively. As a p-type semiconductor, its electronic conductivity is less than 1 S cm^{-1} in 5% H_2-95% Ar. $La_xSr_{1-x}TiO_3$ shows high electronic conductivity of 300-500 S cm^{-1} above 800 °C in reducing atmospheres [7]. However, low catalytic activity and insufficient oxygen ionic conductivity limit its application [8]. In the last two decades, double perovskite oxides with high electrical conductivity, good chemical stability and promising catalytic activity have been studied intensively as anode materials of hydrocarbon fueled SOFCs. A single cell supported by a 300-μm-thick $La_{0.8}Sr_{0.2}Ga_{0.83}Mg_{0.17}O_{2.815}$ electrolyte layer with $Sr_2MgMoO_{6-\delta}$ anode exhibits $P_{\max}$ of 838 and 438 mW cm^{-2} at 800 °C with H_2 and CH_4 as fuels, respectively [9, 10]. The $P_{\max}$ of a similar cell with A-site ordered $PrBaMn_2O_{5+\delta}$ anode fed with H_2 and C_3H_8 at 850 °C reach 1.57 and 0.85 W cm^{-2}, respectively, while only about 0.25 W cm^{-2} is obtained when CH_4 is used as fuel [11]. Doped ferrite perovskites show high catalytic activity to chemical and electrochemical oxidation reactions and have been widely used as anode materials in SOFCs [12-16]. With a double perovskite $Sr_2FeMoO_{6-\delta}$ anode, a single cell supported by a 300-μm-thick $La_{0.9}Sr_{0.1}Ga_{0.8}Mg_{0.2}O_{3-\delta}$ electrolyte layer exhibits a $P_{\max}$ of 0.6 W cm^{-2} at 850 °C using CH_4 as the fuel [17-19]. The $P_{\max}$ of another cell with a similar structure using $La_{0.5}Sr_{0.5}Fe_{0.9}Mo_{0.1}O_{3-\delta}$ as the anode reaches 0.51 W cm^{-2} fueled with CH_4 [14]. At 800 °C, a cell with $(PrBa)_{0.95}(Fe_{0.9}Nb_{0.1})_2O_{5+\delta}$ anode shows $P_{\max}$ of 0.64 and 0.57 W cm^{-2} with wet and dry CH_4 as fuels, respectively [12].

It is well known that the physical and chemical properties of $ABO_{3-\delta}$ perovskites can be tailored with cation doping at A and B sites [20, 21]. Apart from that, the partial substitution of other anions such as N^{3-}, S^{2-}, F^- and Cl^- for O^{2-} is another effective strategy for tuning the properties of metal oxide catalysts such as lattice structure, electronic structure and metal-oxygen bond strength [20]. Lee and Ng [22] found that the doping of F in $YBa_2Cu_3O_{6+x}$ improves the selectivity of methane partial oxidation. Dai et. al investigated F and Cl doped $YBa_2Cu_3O_{7-\delta}$ [23], $La_{1-x}Sr_xFeO_{3-\delta}$ [24] and $La_{1.85}Sr_{0.15}CuO_{4-\delta}$ [25] as the catalysts for selective oxidation of ethane to ethene and found that the incorporation of halide ions enhances the activity and mobility of lattice oxygen, resulting in higher ethane conversion and ethene selectivity [26]. Since fluorine has a higher electronegativity (4.0) than oxygen (3.44) and attracts electrons better [27], the incorporation of F into $ABO_{3-\delta}$ perovskite can reduce the valence electron density of oxygen, weaken metal-oxygen bonds and enhance the bulk diffusion and surface exchange of oxygen significantly [28, 29]. Meanwhile, other properties of perovskite oxides, such as electrical conductivity [30] and thermal expansion coefficient [31], can be also regulated with the doping of F. In recent years, the incorporation of F has been widely used to improve the catalytic activity and stability of perovskite electrode materials for solid oxide fuel/electrolysis cells [32, 33].

La-doped $BaFeO_{3-\delta}$ perovskite oxides have been investigated extensively as ferromagnetic materials [34, 35], oxygen storage materials [36], and also promising SOFC cathode materials [37-41]. $La_{0.05}Ba_{0.95}FeO_{3-\delta}$ shows a high oxygen electrochemical reduction activity comparable with $Ba_{0.5}Sr_{0.5}Co_{0.8}Fe_{0.2}O_{3-\delta}$ [42]. In this work, $La_{0.5}Ba_{0.5}FeO_{3-\delta}$ (LBF) is studied as an anode material for SOFCs with H_2 and CH_4 as fuels. The strategy of F incorporation is applied to accelerate the oxygen surface exchange and thus the electrochemical oxidaiton process. The results show that F-doped LBF is a promising anode material with high catalytic activity and stability.

2. Experimental

2.1. Preparation of Materials

$La_{0.5}Ba_{0.5}FeO_{3-x-\delta}F_x$ ($LBFF_x$, x=0, 0.05, 0.1) anode powders were synthesized through the sol-gel method [11, 43]. Stoichiometric $La(NO_3)_3 \cdot 6H_2O$ (99.9%, Aladdin), $Ba(NO_3)_2$ (99.5%, Aladdin), LaF_3 (99.99%, Aladdin) and $Fe(NO_3)_3 \cdot 9H_2O$ (99.99%, Aladdin) were dissolved in deionized water. Then citric acid (99.5%, Aladdin) and EDTA (99.5%, Aladdin) were added into the solution as complexation agents with a molar ratio of metal cations: citric acid: EDTA of 1: 1.5: 1 at 85 °C under stirring. The pH of the solution was adjusted to 7 with $NH_3 \cdot H_2O$. The gel obtained was slowly decomposed at 350 °C to form a black precursor, which was ground and then calcined at 950 °C for 4 h in the air. $La_{0.4}Ce_{0.6}O_{2-\delta}$ (LDC) anode buffer layer and $Ba_{0.5}Sr_{0.5}Co_{0.8}Fe_{0.2}O_{3-\delta}$ (BSCF) cathode powders were synthesized following the procedures described in previous publications [9, 44].

2.2. Characterization

The X-ray diffraction (XRD) patterns of the $LBFF_x$ powders before and after reduction were recorded at room temperature using a D8 Focus diffractometer (Bruker Corp., Germany), Cu-Kα radiation, 40 kV and 200 mA. The surface properties of the reduced $LBFF_x$ powders were investigated using a Thermo ESCALAB 250Xi X-ray photoelectron spectrometer (XPS) with an Al Kα source (hν = 1486.6 eV). The XPS results were referenced to the C 1s binding energy (284.8 eV). The reduced anode powders were also studied with high-resolution transmission electron microscopy (HRTEM) and high-angle annular darkfield scanning TEM (HAADF-STEM) using a transmission electron microscope (JEOL JEM 2100) with an energy dispersive X-ray (EDX) analyzer. The oxygen nonstoichiometry of the anode powders before reduction was studied with iodometric titration. To evaluate the resistance to coking of the anode materials, the $LBFF_x$ powders were treated in wet CH_4 (100 mL min^{-1}, STP) at 850 °C for 2 h, and then thermogravimetric analysis (TGA) of the samples was carried out using a NETZSCH analyzer (STA, 449F3) in the air from room temperature to 1000 °C at a heating rate of 5 °C min^{-1} to measure the amount of carbon deposition.

The four-probe direct current method was used to measure the electrical conductivities of the samples. The anode powders were pressed into rectangular bars at 250 MPa and then sintered at 1300 °C in air for 4 h to achieve a relative density higher than 99%. Then the electrical conductivities were measured with an electrochemical workstation (VersaSTAT 3, Ametek) in the air and 5% H_2-95% Ar, respectively. The electrical conductivity relaxation (ECR) behavior was recorded when the atmosphere was switched from 5% H_2-95% Ar to 20% H_2-80% Ar.

2.3. Cell Fabrication and Test

For the symmetric cells, $La_{0.8}Sr_{0.2}Ga_{0.8}Mg_{0.2}O_{3-\delta}$ (LSGM) electrolyte powder (Fuel cell materials Co., USA) was pressed into pellets, and then sintered in air at 1450 °C for 20 h. $LBFF_x$ and LDC powders were mixed with a binder (V006, Heraeus Ltd.) to form slurries. The LDC slurry was screen-printed on the both sides of the electrolyte layer and sintered at 1400 °C for 2 h as buffer layers to avoid the interaction between the LSGM electrolyte and the $LBFF_x$ electrodes [9, 45, 46]. The anode slurry was printed on the LDC layers and then calcined at 950 °C in air for 4 h. The geometrical area of the anode was 0.5 cm^2. Ag paste was used as the current collector. The electrochemical impedance spectra (EIS) of the symmetric cells were recorded from 1 MHz to 0.1 Hz with an amplitude of 10 mV using the electrochemical workstation under various H_2 partial pressures (P_{H2}) with Ar as the balance gas.

The fabrication procedure of single cells was similar to that of the symmetric cells. After the $LBFF_x$ | LDC | LSGM half cell was fabricated, the BSCF slurry was screen-printed on the other side of the electrolyte layer, and then sintered at 950 °C in air for 4 h. *I-V* and *I-P* curves of the cells were measured with the electrochemical workstation with wet H_2 and CH_4 (with 3% H_2O) as fuels and oxygen as oxidant. The flow rates of all the gases were 100 ml min^{-1} (STP).

3. Results and Discussion

3.1. Phase composition and structure

The XRD patterns of LBF, $La_{0.5}Ba_{0.5}FeO_{2.95-\delta}F_{0.05}$ ($LBFF_{0.05}$) and $La_{0.5}Ba_{0.5}FeO_{2.9-\delta}F_{0.1}$ ($LBFF_{0.1}$) anode powders are shown in Figure 1. LBF with the Goldschmidt tolerance factor (*t*) close to 1 (Table S1) shows a cubic perovskite structure with a space group of *Pm*-3*m* before reduction (Figure 1a), which is consistent with the structure of $La_{0.5}Ba_{0.5}FeO_{2.955}$ (JCPDS #80-1054). The *t* remains almost unchanged after the incorporation of F on the anion site, and the perovskite structure is maintained without any impure phase. However, the characteristic peaks shift slightly to higher angles, indicating a tiny contraction of the unit cells (Table S2) due to the smaller ionic radius of F^- (1.33 Å) vs. O^{2-} (1.4 Å). No phase change is observed after the reduction of the samples at 850 °C in 5% H_2-95% Ar for

10 h (Figure 1b). Nevertheless, the peaks move to lower angles after reduction, corresponding to an expansion of the lattice (Table S3). The reduction of Fe ions enhances electrostatic repulsion, resulting in the expansion of the unit cells [47].

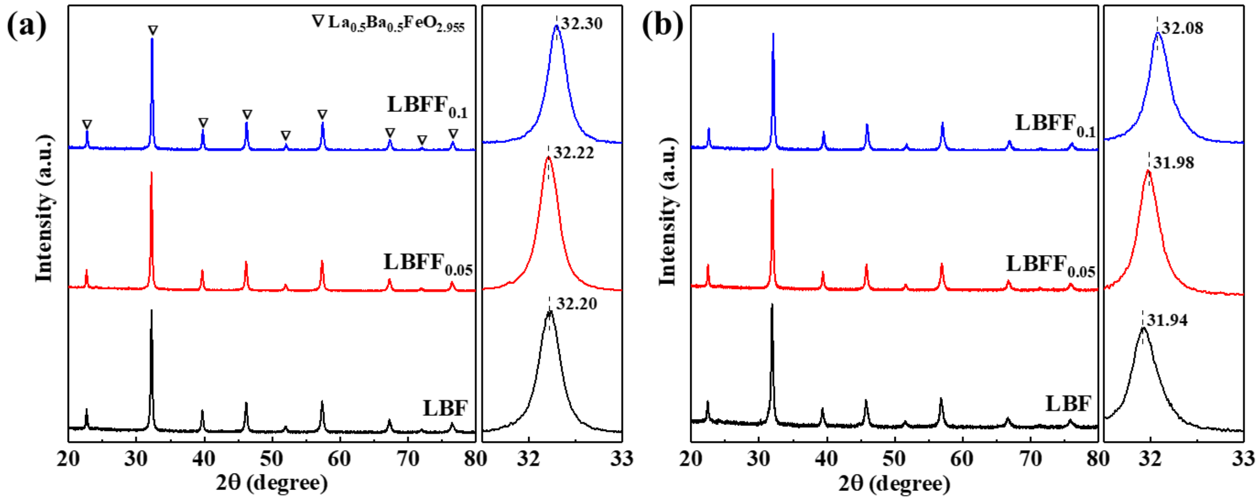

Figure 1. XRD patterns of various anode powders (a) before and (b) after reduction at 850 °C in 5% H_2-95% Ar for 10 h.

3.2. Chemical composition and microstructure

XPS of the anode powders were measured to verify the successful doping of F^- into the perovskite lattice. La, Ba, Fe and O are detected in LBF (Figure 2a). With the addition of F, a weak peak at around 684 eV is observed, which is characteristic of F 1s signal [48]. Figure 2b shows the STEM images and corresponding EDX mapping of $LBFF_{0.1}$ powder after reduction. La, Ba, Fe, O and F are all distributed homogeneously in the anode. The particle size of the reduced $LBFF_{0.1}$ is 100-200 nm (Figure 2c). The HRTEM image and the corresponding fast Fourier transform pattern along the [1 1 1] direction are shown in Figure 2d. The distance between the adjacent fringes is 0.277 nm, corresponding to the d-spacing of (1 1 0) plane of LBF.

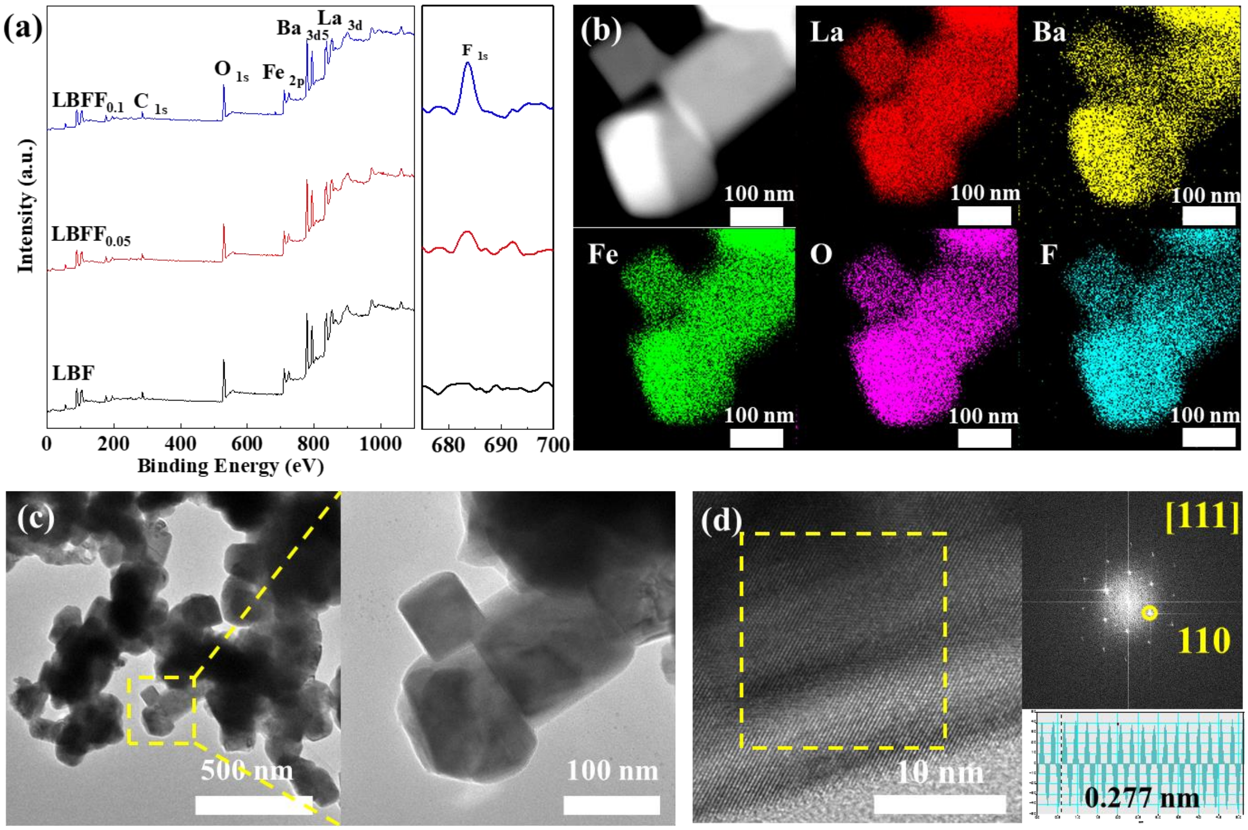

Figure 2. (a) XPS full survey spectra and magnified XPS spectra of F 1s of the anode powders; (b) STEM image and EDS elemental mappings; (c) TEM image and (d) HRTEM image of $LBFF_{0.1}$ powder.

3.3. Oxygen nonstoichiometry and valence of the transition metals

With the increase of F content from 0 to 0.1, the oxygen nonstoichiometry (δ) of $LBFF_x$ samples before reduction measured via iodometry technique decreases from 0.176 to 0.118 (Figure S1), which indicates that part of F ions takes the place of the oxygen vacancies (Figure S2). Meanwhile, the average valence of Fe increases slightly from 3.148 to 3.163. The decrease of oxygen vacancy and the increase of Fe valence are also found in other ferrite perovskites with the doping of F [29]. The deconvolved O 1s spectra of the reduced anode materials are shown in Figure 3a. The two peaks at about 528.6 and 531.1 eV correspond to lattice oxygen (O_{latt}) and adsorbed oxygen (O_{ad}), respectively.

With the doping of F, more O_{latt} and less O_{ad} are observed (Table 1), indicating the decrease of oxygen vacancy concentration, which is in consistence with the iodometry results. Besides, the binding energy of O_{latt} increases slightly, implying a lower valence electron density of O_{latt} since the electronegativity of F is higher than that of O [23-25]. Therefore, the Coulombic force between the B-site cations and O_{latt} will be weaken, resulting in more active O_{latt} [49].

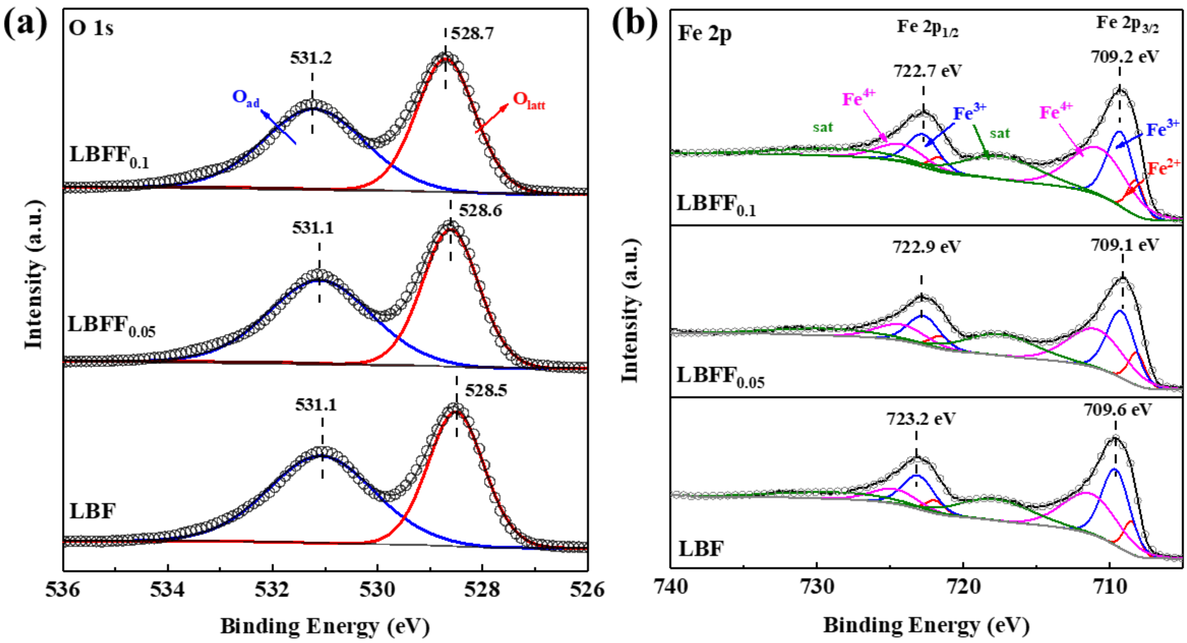

Figure 3. XPS of (a) O 1s and (b) Fe 2p of the $LBFF_x$ powders after reduction.

The Fe 2p core-level spectra of the anode samples after reduction are presented in Figure 3b. The peaks at the binding energies of about 723 and 709 eV are assigned to Fe $2p_{1/2}$ and Fe $2p_{3/2}$, respectively. With the doping of F, those two peaks shift generally to lower binding energies, implying a lower Fe-O bond energy, which could facilitate both bulk diffusion and surface exchange of oxygen [28, 29]. The peaks corresponding to Fe^{4+}, Fe^{3+} and Fe^{2+} are observed in the deconvoluted curves, and the average valence state of Fe (Fe_{ave}) is changed negligibly with the doping of F (Table 1).

Table 1. Percentages of Fe and O species and the average valence state of Fe on the surface of the reduced anode powders obtained from the XPS results.

Sample	O		Fe			
	O_{latt}	O_{ad}	Fe^{2+}	Fe^{3+}	Fe^{4+}	Fe_{ave}
$LBFF_{0.1}$	49.45%	50.55%	8.4%	56.44%	35.16%	3.27
$LBFF_{0.05}$	47.65%	52.35%	9.28%	57.24%	33.48%	3.24
LBF	45.06%	54.94%	8.19%	60.46%	31.36%	3.23

3.4 Electrochemical properties

The electrical conductivities of the anodes in air increase with the rise of temperature at low temperatures (Figure S3), revealing a small polaron behavior (equation 1) similar with other Fe-based perovskite oxides such as $La_{0.6}Sr_{0.4}Co_{0.2}Fe_{0.8}O_{3-\delta}$ [50] and $La_{0.5}Sr_{0.5}Fe_{0.9}Nb_{0.1}O_{3-\delta}$.[51].

$$\sigma = \left(\frac{A}{kT}\right)\exp(-Ea/kT) \quad [1]$$

The conductivities reach 80-100 S cm^{-1} at about 500 °C, and then decrease at higher temperatures probably due to the semiconductor-metal transition, which has been also reported in other perovskites containing Fe [52]. Meanwhile, since $LBFF_x$ are p-type semiconductors in oxidizing atmospheres, the loss of O_{latt} at higher temperatures results in the decrease of the concentration of electron holes (equation 2), which also leads to the decrease of electrical conductivity.

$$O_O^{\times}+2Fe_{Fe}^{\bullet} \leftrightarrow 2Fe_{Fe}^{\times}+1/2O_2+V_O^{\bullet\bullet} \quad [2]$$

The electrical conductivities of the anodes in 5% H_2-95% Ar are much lower than those in air (Figure S4). The conductivities of LBF, $LBFF_{0.05}$, and $LBFF_{0.1}$ are 0.51, 0.60 and 0.68 S cm^{-1} at 850

^{o}C, respectively, which decreases with the lowering of temperature. The conductivities of the anodes increase when the atmosphere is switched from 5% H_2-95% Ar to 20% H_2-80% Ar, which leads to the decrease of the oxygen partial pressure by about one order of magnitude (Table S4), indicating that the n-type conducting behavior dominates in reducing atmospheres. The ECR processes of the samples during the variation of the atmosphere from 5% H_2-95% Ar to 20% H_2-80% Ar are presented in Figure 4a. The re-equilibrium of oxygen in LBF takes about 5700 s at 650 ^{o}C, which is shorten to about 1600 s when the temperature rises to 850 ^{o}C. The relaxation time is significantly reduced with the doping of F. The ECR process consists of two steps, i.e., oxygen surface exchange and bulk diffusion. In this work, the bulk diffusion of oxygen is relatively fast since the conduction path is short, and the re-equilibrium process is dominated by the surface reaction. The oxygen surface exchange coefficients (k) of the samples are shown in Figure 4b. The k of LBF at 650 and 850 ^{o}C are about 5×10^{-5} and 1.4×10^{-4} cm s^{-1}, respectively. The doping of F results in the increase of k probably due to the lowering of Fe-O bond energy (Figure 3b). The k of $LBFF_{0.1}$ are about 1.9×10^{-4}, 2.4×10^{-4} and 2.8×10^{-4} cm s^{-1} at 750, 800 and 850 ^{o}C, respectively, comparable to other excellent electrode materials such as $Sr_2Fe_{1.5}Mo_{0.5}O_{6-\delta}$ (2.3×10^{-4} cm s^{-1} at 750 ^{o}C) [53], SDC (1.4×10^{-5} - 1.8×10^{-5} cm s^{-1} at 800 ^{o}C) [54, 55] and Ni-SDC cermet (1.1×10^{-4} - 3.9×10^{-4} cm s^{-1} at 800 ^{o}C) [55]. Meanwhile, the activation energies (E_a) for the k of $LBFF_x$ are quite low (0.31-0.46 eV), which will facilitate the electrochemical oxidation of the fuels.

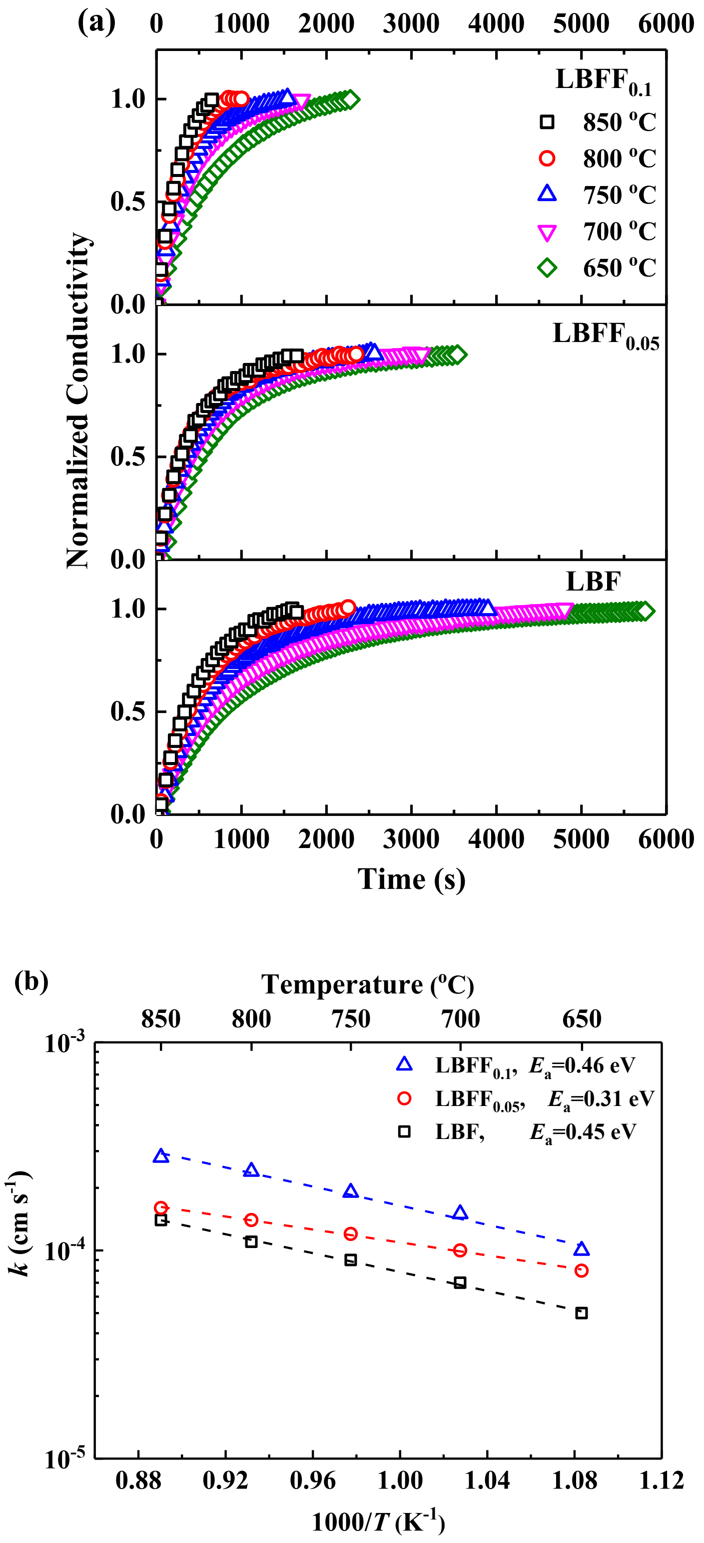

Figure 4. (a) Normalized conductivity relaxation profiles of the LBFF$_x$ samples at various temperature; (b) Oxygen surface reaction rate constant (k) values of the LBFF$_x$ samples.

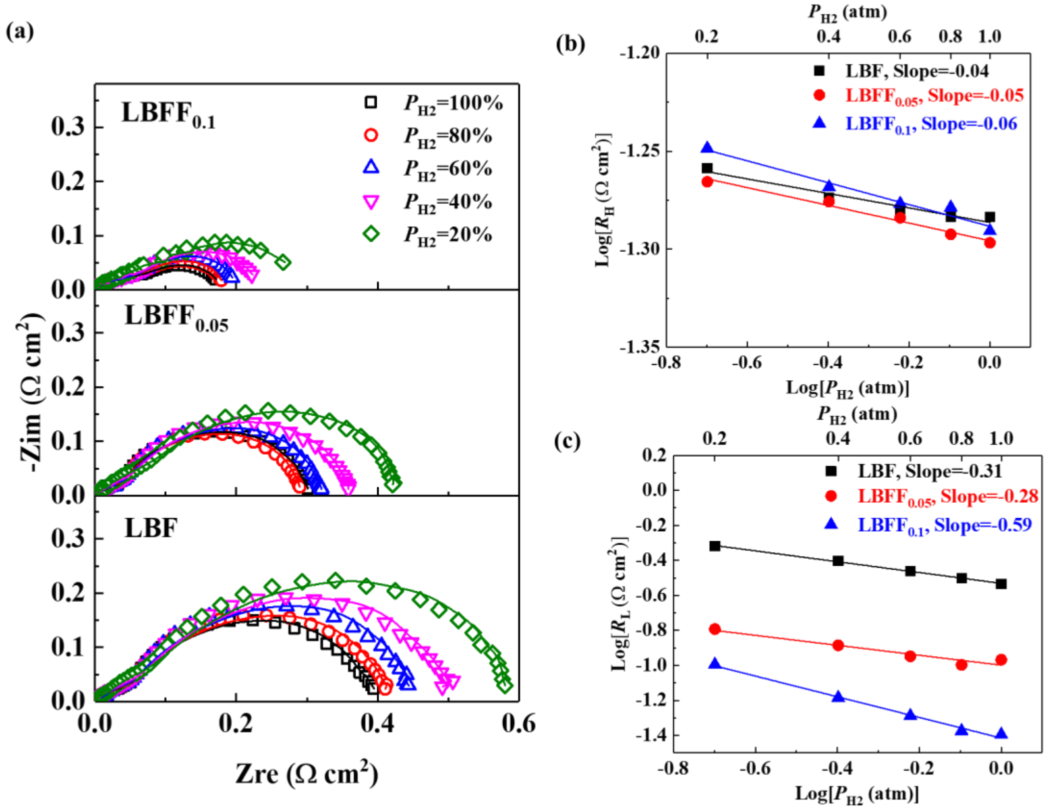

Figure 5. (a) Nyqusit plots of the symmetric cells with different anodes at 850 °C under various P_{H2}; (b) R_H and (c) R_L of the symmetric cells under various P_{H2} at 850 °C.

The EIS results of the symmetric cells with various anodes at 850 °C are shown in Figure 5a. The ohmic resistances (R_o) of the cells were deducted, and the arcs corresponding to the electrode processes are fitted with an equivalent circuit (R_HCPE$_H$)(R_LCPE$_L$). R_H and R_L are the polarization resistances (R_p) of the symmetric cells in the high frequency (HF, about 10^4-10^1 Hz) and low frequency (LF, about 10^1-10^{-2} Hz) ranges, respectively, and CPE$_H$ and CPE$_L$ are the corresponding constant phase elements. R_p of LBF, LBFF$_{0.05}$ and LBFF$_{0.1}$ anodes in H_2 are 0.20, 0.15 and 0.08 Ω cm^2, respectively. R_H of the anodes are similar (Figure 5b), while R_L of the anode decreases significantly with the doping of F (Figure 5c). For LBF and LBFF$_{0.05}$, their R_L are much higher than R_H, indicating that the rate of H_2 electrochemical oxidation is limited by the LF process. In contrast, R_L of LBFF$_{0.1}$ is lower than R_H since the addition of F accelerates the LF process remarkably.

For a better understanding of the anode process, the EIS of the cells were tested under various P_{H2}. For all the anodes, the decrease of P_{H2} results in the rise of both R_H and R_L, and linear relationships are revealed between Log$R$ and LogP_{H2}. The electrochemical oxidation of H_2 on the surface of the LBFF$_x$ anodes can be roughly divided into a series of main steps [56, 57], which start from the dissociative adsorption of H_2 on the surface of the anode (step 1), and its rate is proportional to P_{H2}. Parallelly, lattice oxygens transfer in the anode from bulk to surface via oxygen vacancies (step 2), followed by the surface exchange of oxygen (step 3), which are not influenced by P_{H2}. Then, the charge transfer reactions, i.e., the electrochemical oxidation of the adsorbed hydrogen (steps 4-5), happen on the anode surface. If those are the rate-determining steps (RDS), the slope of the Log$R$-LogP_{H2} curve should be about -0.5. Finally, there is the desorption of H_2O product (step 6), a step not affected by P_{H2}. The slopes of LogR_H-LogP_{H2} curves of the anodes are between -0.04 and -0.06, demonstrating that the bulk conduction of oxygen (step 2) is the RDS of the HF process. The slopes of LogR_L-LogP_{H2} curves of LBF and LBFF$_{0.05}$ anodes are about -0.30, implying mixed RDS of oxygen surface exchange (step 3) and charge transfer reactions (steps 4-5). With the addition of F, the surface exchange of oxygen is accelerated (Figure 4b), which is no longer the RDS, resulting in the slope of -0.59 for LBFF$_{0.1}$ anode.

Step 1. $\mathrm{H_2\ (g)} \leftrightarrow 2\mathrm{H_{surf}}$, $R \propto P_{\mathrm{H2}}^{-1}$

Step 2. $\mathrm{O^{\times}_{O,\ bulk}} + \mathrm{V^{\bullet\bullet}_{O,surf}} \leftrightarrow \mathrm{O^{\times}_{O,surf}} + \mathrm{V^{\bullet\bullet}_{O,bulk}}$, $R \propto P_{\mathrm{H2}}^{0}$

Step 3. $\mathrm{O^{\times}_{O,surf}} \leftrightarrow \mathrm{V^{\bullet\bullet}_{O,surf}} + \mathrm{O^{2-}_{surf}}$, $R \propto P_{\mathrm{H2}}^{0}$

Step 4. $\mathrm{H_{surf}} + \mathrm{O^{2-}_{surf}} \leftrightarrow \mathrm{OH^{-}_{surf}} + e^{-}$, $R \propto P_{\mathrm{H2}}^{-\frac{1}{2}}$

Step 5. $\mathrm{H_{surf}} + \mathrm{OH^{-}_{surf}} \leftrightarrow \mathrm{H_2O_{surf}} + e^{-}$, $R \propto P_{\mathrm{H2}}^{-\frac{1}{2}}$

Step 6. $\mathrm{H_2O_{surf}} \leftrightarrow \mathrm{H_2O\ (g)}$, $R \propto P_{\mathrm{H2}}^{0}$

The cross-sectional scanning electron microscope (SEM) image of the cell with $LBFF_{0.1}$ anode is shown in Figure S6. The thicknesses of the porous anode and $La_{0.4}Ce_{0.6}O_{2-\delta}$ (LDC) buffer layers are about 40 and 15 μm, respectively. Tight contact between the anode, the buffer and the dense LSGM electrolyte layers is observed. The open circuit voltages (OCVs) of the cells reach about 1.1 V at 850 °C with wet H_2 as the fuel (Figure 6a). The cell with LBF anode shows a maximum power density (P_{max}) of 1446 mW cm^{-2}. With the doping of F in the anode, the P_{max} of the cell increases remarkably due to the acceleration of the oxygen surface exchange process (Figure 4). With $LBFF_{0.1}$ as the anode, the cell exhibits a P_{max} of 1860 mW cm^{-2}, much higher than other cells with similar configurations reported previously (Table S5). The EIS results of the single cells are shown in Fig. S6a. R_o of the cells are about 0.12-0.15 Ω cm^2, while R_p shows an order of $LBFF_{0.1} < LBFF_{0.05} < LBF$. When the temperature drops to 800 and 750 °C, the decreases to 1173 and 742 mW cm^{-2}, respectively (Figure 6b).

The OCVs of the cells fed with wet CH_4 are about 1.0 V at 850 °C (Figure 6c) [12]. The P_{max} of 691, 768 and 809 mW cm^{-2} are obtained by the cells with LBF, $LBFF_{0.05}$ and $LBFF_{0.1}$ anodes, respectively. The lower polarization resistance with the doping of F indicates the improvement of the catalytic activity of the anode towards the electrochemical oxidation of CH_4 (Figure S6b). The CH_4 temperature-programmed surface reaction result also proves that the doping of F improves the catalytic activity of LBF to methane oxidation (Figure S7). The single cell with $LBFF_{0.1}$ anode exhibits P_{max} of 573 and 335 mW cm^{-2} at 800 and 750 °C, respectively (Figure 6d). The performance of the cell with $LBFF_{0.1}$ anode is among the best in those of the cells with perovskite anodes and LSGM electrolytes (Table S5).

The short-term stability of the cell with $LBFF_{0.1}$ anode fed with wet CH_4 at 850 °C under a constant output current density of 100 mA cm^{-2} is shown in Figure 7a. No obvious degradation is observed during the 40 h test. To evaluate the coking resistance of $LBFF_x$, all the anode powders were treated in wet CH_4 at 850 °C for 2 h, and the amount of carbon deposits was measured with thermogravimetric analysis (TGA) in the air. As shown in Figure 7b, the weight losses of LBF, $LBFF_{0.05}$ and $LBFF_{0.1}$ are around 1.5 wt%, similar to that of the $LBFF_{0.1}$ powder without coking treatment (bare $LBFF_{0.1}$), suggesting that the weight losses are mainly due to the loss of lattice oxygen with the rise of temperature, while the carbon deposition is negligible. Figure 7c and 7d are the SEM images of the $LBFF_{0.1}$ anode surface before and after the 40 h stability test, respectively. No carbon is observed after the test, proving that $LBFF_{0.1}$ has a high coking resistance and is a promising anode material for SOFCs with CH_4 as the fuel.

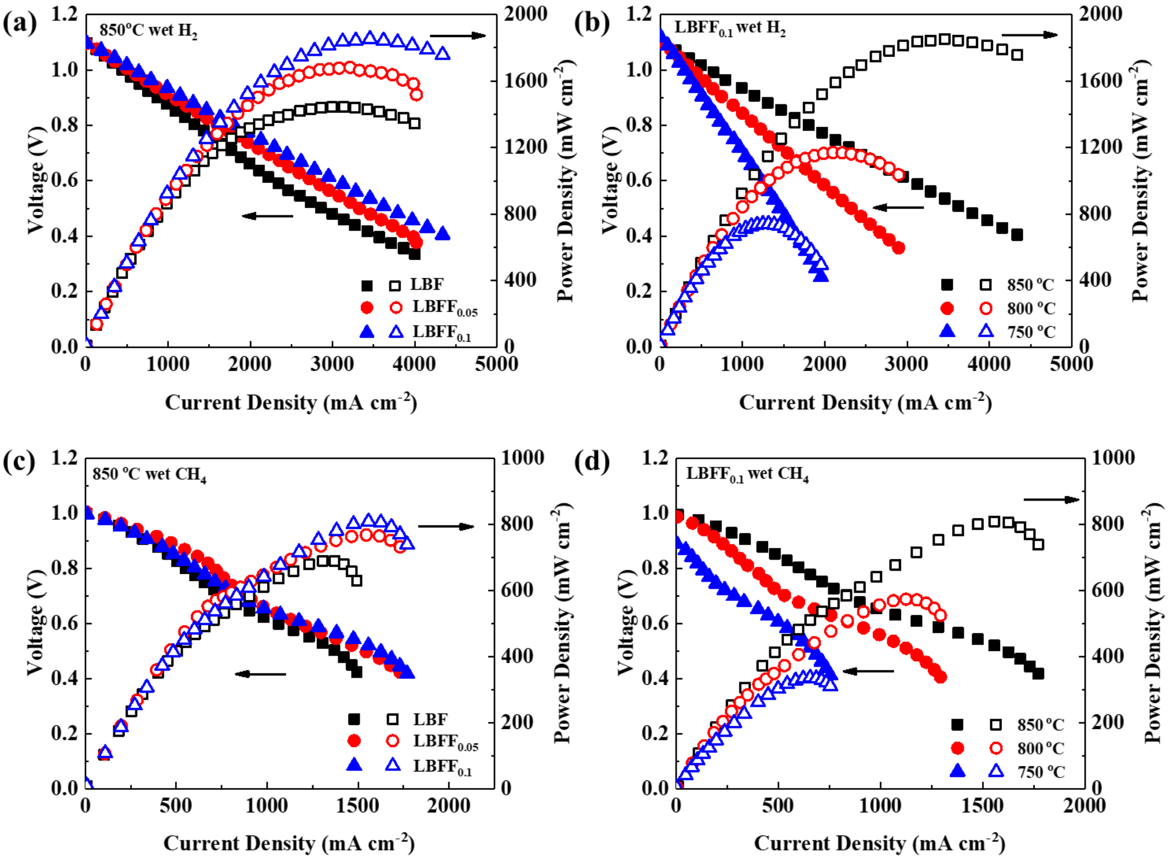

Figure 6. *I-V* and *I-P* curves of single cells (a) with various anodes at 850 °C and (b) with $LBFF_{0.1}$ anode at various temperatures with wet H_2 as fuel, (c) with various anodes at 850 °C and (d) with $LBFF_{0.1}$ anode at various temperatures with wet CH_4 as fuel.

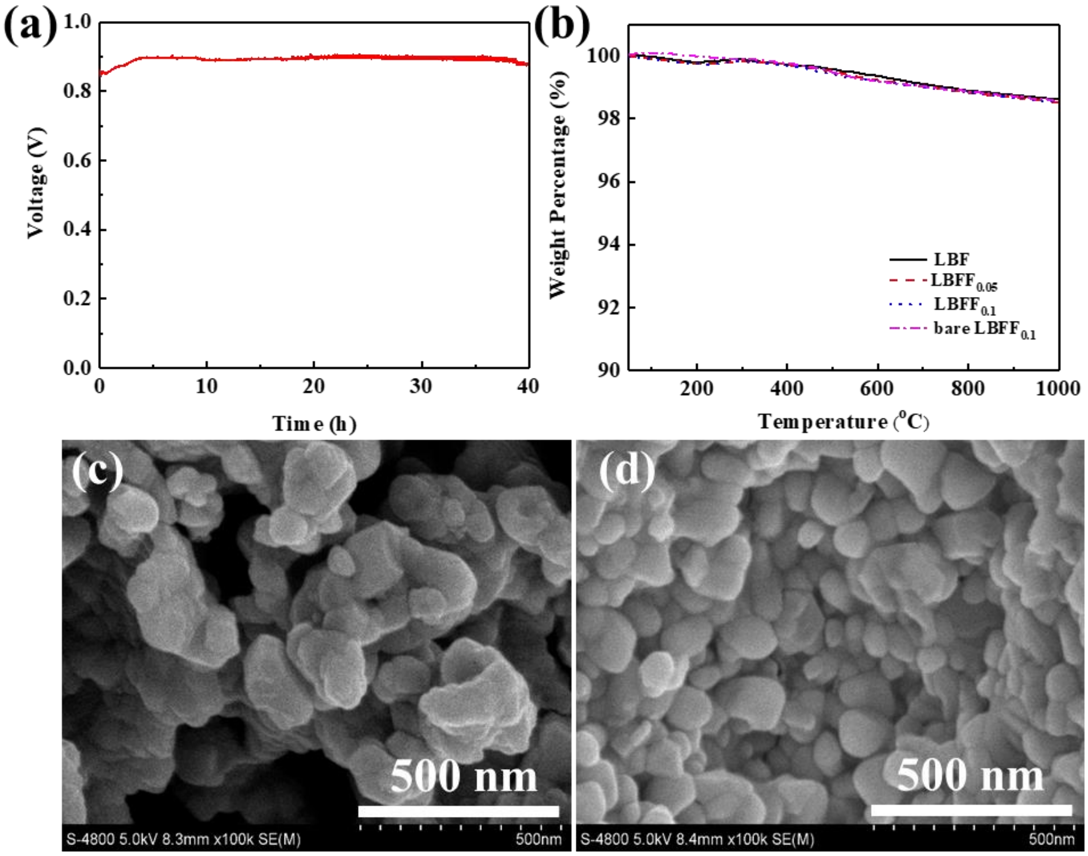

Figure 7. (a) The durability of the cell with $LBFF_{0.1}$ anode discharged at 100 mA cm^{-2} at 850 ºC with wet CH_4 as fuel; (b) TGA curves of various anodes in the air before and after carbon deposition; SEM images of the $LBFF_{0.1}$ anode surface of the cell (c) before and (d) after the durability test.

4. Conclusion

In this work, $La_{0.5}Ba_{0.5}FeO_{3-\delta}$ doped with F on the anion sites is synthesized through the sol-gel method and studied as an anode material of SOFCs. $LBFF_x$ (x = 0-0.1) shows a stable pure cubic perovskite structure both in oxidizing and reducing atmospheres. The doping of F results in less oxygen vacancies and a slightly higher electrical conductivity in the reducing atmosphere. The incorporation of F also weakens the bonds between cations and oxygen ions, and thus accelerates the surface exchange of oxygen, which is one of the RDS of the anode reaction. The R_p of LBF, $LBFF_{0.05}$ and $LBFF_{0.1}$ anodes at 850 °C with wet H_2 as fuel are 0.20, 0.15 and 0.08 Ω cm^2, respectively. The P_{max} of the single cell with $LBFF_{0.1}$ anode and a 300 μm-thick LSGM electrolyte layer reaches 1860 and 809 mW cm^{-2} at 850 °C with wet H_2 and CH_4 as fuels, respectively. The $LBFF_{0.1}$ anodes also show a high coking resistance, and a stable power output for 40 h is obtained with wet methane as fuel.

Acknowledgements

The financial support from National Natural Science Foundation of China under contract number 22075205 and the support of Tianjin Municipal Science and Technology Commission under contract number 19JCYBJC21700 are gratefully acknowledged. The work has been also supported by the Program of Introducing Talents to the University Disciplines under file number B06006, and the Program for Changjiang Scholars and Innovative Research Teams in Universities under file number IRT 0641.

References

[1] N. Mahato, A. Banerjee, A. Gupta, S. Omar, K. Balani, Prog. Mater Sci., 72 (2015) 141-337.

[2] Y. Yang, H. Bao, H. Ni, X. Ou, S. Wang, B. Lin, P. Feng, Y. Ling, J. Power Sources, 482 (2021) 228959.

[3] T.M. Gür, Prog. Energy Combust. Sci., 54 (2016) 1-64.

[4] S. Mcintosh, R.J. Gorte, Chem. Rev., 104 (2004) 4845-4865.

[5] P. Boldrin, E. Ruiz-Trejo, J. Mermelstein, J.M. Bermudez Menendez, T. Rami Rez Reina, N.P. Brandon, Chem. Rev., 116 (2016) 13633-13684.

[6] S. Tao, J.T. Irvine, Nat. Mater., 2 (2003) 320-323.

[7] O.A. Marina, N.L. Canfield, J.W. Stevenson, Solid State Ion., 149 (2002) 21-28.

[8] J. Li, T. Lv, N. Hou, P. Li, X. Yao, L. Fan, T. Gan, Y. Zhao, Y. Li, Int. J. Hydrogen Energy, 42 (2017) 22294-22301.

[9] Y.H. Huang, R.I. Dass, Z.L. Xing, J.B. Goodenough, Science, 37 (2006) 254-257.

[10] Y.-H. Huang, R.I. Dass, J.C. Denyszyn, J.B. Goodenough, J. Electrochem. Soc., 153 (2006) A1266-A1272.

[11] S. Sengodan, S. Choi, A. Jun, T.H. Shin, Y.W. Ju, H.Y. Jeong, J. Shin, J.T. Irvine, G. Kim, Nat. Mater., 14 (2015) 205-209.

[12] H. Ding, D. Zhou, S. Liu, W. Wu, Y. Yang, Y. Yang, Z. Tao, Appl. Energy, 233-234 (2019) 37-43.

[13] L. Zhao, K. Chen, Y. Liu, B. He, J. Power Sources, 342 (2017) 313-319.

[14] F. Liu, L. Zhang, G. Huang, B. Niu, X. Li, L. Wang, J. Zhao, Y. Jin, Electrochim. Acta, 255 (2017) 118-126.

[15] H. Ding, Z. Tao, S. Liu, J. Zhang, Sci. Rep., 5 (2015) 18129.

[16] W. He, X. Wu, F. Dong, M. Ni, J. Power Sources, 363 (2017) 16-19.

[17] Z. Wang, Y. Tian, Y. Li, J. Power Sources, 196 (2011) 6104-6109.

[18] B. Li, S. He, J. Li, X. Yue, J.T.S. Irvine, D. Xie, J. Ni, C. Ni, ACS Catal., (2020) 14398-14409.

[19] S. Liu, K.T. Chuang, J.-L. Luo, ACS Catal., 6 (2015) 760-768.

[20] Y. Liu, W. Wang, X. Xu, J.-P. Marcel Veder, Z. Shao, J. Mater. Chem. A, 7 (2019) 7280-7300.

[21] Q. Yang, G. Wang, H. Wu, B.A. Beshiwork, D. Tian, S. Zhu, Y. Yang, X. Lu, Y. Ding, Y. Ling, Y. Chen, B. Lin, J. Alloys Compd., 872 (2021) 159633.

[22] I. Lee, K. Ng, Catal. Lett., 2 (1989) 403-412.

[23] H.X. Dai, C.F. Ng, C.T. Au, J. Catal., 193 (2000) 65-79.

[24] H. Dai, C. Ng, C. Au, J. Catal., 189 (2000) 52-62.

[25] H.X. Dai, C.F. Ng, C.T. Au, J. Catal., 197 (2001) 251-266.

[26] H. Chang, E. Bjørgum, O. Mihai, J. Yang, H.L. Lein, T. Grande, S. Raaen, Y.-A. Zhu, A. Holmen, D. Chen, ACS Catal., 10 (2020) 3707-3719.

[27] L. Pauling, J. Am. Chem. Soc., 54 (1932) 3570-3582.

[28] J. Zhu, G. Liu, Z. Liu, Z. Chu, W. Jin, N. Xu, Adv. Mater., 28 (2016) 3511-3515.

[29] Z. Zhang, Y. Zhu, Y. Zhong, W. Zhou, Z. Shao, Adv. Energy Mater., 7 (2017) 1700242.

[30] Y. Liu, X. Meng, F. Yu, M. Yin, N. Yang, B. Meng, M.V. Sofianos, S. Liu, Int. J. Hydrogen Energy, 43 (2018) 12328-12336.

[31] Y. Wan, Y. Xing, Y. Li, D. Huan, C. Xia, J. Power Sources, 402 (2018) 363-372.

[32] Y. Li, Y. Li, Y. Wan, Y. Xie, J. Zhu, H. Pan, X. Zheng, C. Xia, Adv. Energy Mater., 9 (2019) 1803156.

[33] W. Wang, X. Zhang, D. Zhang, Q. Zeng, Y. Jiang, B. Lin, Ceram. Int., 46 (2020) 23964-23971.

[34] S. Zhang, S. Tan, L. Pi, Y. Zhang, J. Magn. Magn. Mater., 322 (2010) 3381-3384.

[35] I. Fita, A. Wisniewski, R. Puzniak, P. Iwanowski, V. Markovich, S. Kolesnik, B. Dabrowski, Phys. Rev. B, 95 (2017) 134428.

[36] J.W. Lekse, S. Natesakhawat, D. Alfonso, C. Matranga, J. Mater. Chem. A, 2 (2014) 2397–2404.

[37] F. Bidrawn, S. Lee, J.M. Vohs, R.J. Gorte, J. Electrochem. Soc., 155 (2008) B660-B665.

[38] A. Ecija, K. Vidal, A. Larrañaga, M.L. No, A. Laresgoiti, M.I. Arriortua, ECS Trans., 25 (2009) 2639-2644.

[39] D. Chen, F. Wang, H. Shi, R. Ran, Z. Shao, Electrochim. Acta, 78 (2012) 466-474.

[40] D. Chen, C. Chen, F. Dong, Z. Shao, F. Ciucci, J. Power Sources, 250 (2014) 188-195.

[41] S. Nasri, A.L. Ben Hafsia, M. Tabellout, M. Megdiche, RSC Adv., 6 (2016) 76659-76665.

[42] F. Dong, D. Chen, Y. Chen, Q. Zhao, Z. Shao, J. Mater. Chem., 22 (2012) 15071.

[43] Y.-F. Sun, Y.-Q. Zhang, B. Hua, Y. Behnamian, J. Li, S.-H. Cui, J.-H. Li, J.-L. Luo, J. Power Sources, 301 (2016) 237-241.

[44] Z. Shao, S.M. Haile, Nature, 431 (2004) 170-173.

[45] Y. Lin, S.A. Barnett, Electrochem. Solid-State Lett., 9 (2006) A285.

[46] J.-H. Wan, J.Q. Yan, J.B. Goodenough, J. Electrochem. Soc., 152 (2005) A1511.

[47] E. Jedvik, A. Lindman, M.Þ. Benediktsson, G. Wahnström, Solid State Ion., 275 (2015) 2-8.

[48] E.J. Moon, Y. Xie, E.D. Laird, D.J. Keavney, C.Y. Li, S.J. May, J. Am. Chem. Soc., 136 (2014) 2224-2227.

[49] J. Feng, J. Qiao, W. Wang, Z. Wang, W. Sun, K. Sun, Electrochim. Acta, 215 (2016) 592-599.

[50] Y. Liu, S. Hashimoto, H. Nishino, K. Takei, M. Mori, J. Power Sources, 164 (2007) 56-64.

[51] L. Bian, C. Duan, L. Wang, L. Zhu, R. O'Hayre, K.-C. Chou, J. Power Sources, 399 (2018) 398-405.

[52] J. Liu, J. Ding, L. Miao, Z. Gong, K. Li, W. Liu, J. Alloys Compd., 786 (2019) 163-168.

[53] B. Hu, Y. Wang, Z. Zhu, C. Xia, H.J. Bouwmeester, J. Mater. Chem. A, 3 (2015) 10296-10302.

[54] C.B. Gopal, S.M. Haile, J. Mater. Chem. A, 2 (2014) 2405-2417.

[55] M. Zheng, J. Gao, C. Xia, Solid State Ion., 319 (2018) 92-97.

[56] J. Hanna, W.Y. Lee, Y. Shi, A.F. Ghoniem, Prog. Energy Combust. Sci., 40 (2014) 74-111.

[57] X. Zhi, T. Gan, N. Hou, L. Fan, T. Yao, J. Wang, Y. Zhao, Y. Li, J. Power Sources, 423 (2019) 290-296.